Morphology of Layered Silicate− (NanoClay−) Polymer Nanocomposites by Electron Tomography and Small-Angle X-ray Scattering

Lawrence F. Drummy,*,†,‡ Y. C. Wang,§ Remco Schoenmakers,§ Keith May,|| Mike Jackson,○ Hilmar Koerner,†,# B. L. Farmer,† Benji Mauryama,† and Richard A. Vaia†

Materials and Manufacturing Directorate, Air Force Research Laboratory, AFRL/RXBP, 2941 Hobson Way, Wright-Patterson AFB, Ohio 45433, UES Inc., Dayton, Ohio 45432, FEI Company, Hillsboro, Oregon 97124, Triune Software, Beavercreek, Ohio 45431, Innovative Management and Technology Services, Fairmount, West Virginia 26554, and Universal Technology Corporation, Dayton, Ohio 45432

Received October 5, 2007; Revised Manuscript Received December 19, 2007

ABSTRACT: A basis for quantitative analysis of layered silicate− (nanoclay−) polymer nanocomposite morphology using two characterization methods, electron tomography and small-angle X-ray scattering (SAXS), is provided. For tilt greater than 15°, the contrast of a single montmorillonite layer experimentally decreases below the detectable limit of high-angle annular dark-field scanning transmission electron microscopy (HAADF−STEM). Calculations based on *Z*-contrast imaging of a 1 nm thick aluminosilicate layer predict this tilt angle (15°) should produce 17% contrast, consistent with a reasonable limit of HAADF−STEM detection for this system. This result implies that segmentation or thresholding of 2-dimensional *Z*-contrast projection images of randomly oriented, highly anisotropic nanoparticles, such as layered silicates in polymer nanocomposites, will be extremely inaccurate. For example, nearly 75% of the volume of montmorillonite layers in an epoxy matrix will not be identified in the segmentation, owing to their orientation alone. Using electron tomography, this number is reduced to below 15% and tomographic reconstruction reveals three-dimensional information. The corresponding 3D fast Fourier transformation (FFT) indicates that the image volume (10^{-1} μm^3) does not contain sufficient distribution of local environments (interlayer correlation length ∼ 16.1 nm) to directly correspond to the global average as revealed by SAXS (scattering volume, 10^7 μm^3; interlayer correlation length ∼ 12.3 nm). Nevertheless, in contrast to SAXS, the tomographic reconstruction provides precise details of the distribution of morphological features, in addition to statistical averages over the sample volume.

I. Introduction

Polymer nanocomposites (PNCs) are of significant interest for a wide array of applications including sensors,[1] barrier materials[2] and high performance aerospace components.[3] PNCs can be defined as multiphase inorganic/organic hybrid materials in which one of the constituents has at least one dimension on the nanometer length scale (<100 nm). Many natural materials, such as bone,[4] conch shells,[5] or diatoms[6] also belong to this class of materials. Arguably, the most examined class of PNCs are those containing layered aluminosilicates (nanoclays).[7] They consist of pseudo-two-dimensional crystalline aluminosilicate layers[8] dispersed in a polymer matrix. Compared to traditional micro or millimeter scale composite materials, large improvements in several property areas can be engineered with the addition of a very small volume fraction of layered silicate owing to the small dimension (1 nm thickness) and high aspect ratio (>100) of the layers.[9]

While these improvements have been impressive in certain select cases, in many instances PNC properties fail to meet such lofty expectations. There are several possible reasons for this, two of which are insufficient control of the interface between the nanoparticle and the matrix, and inability to reproducibly create and quantitatively verify uniform morphologies. For example, mediocre increases in mechanical performance may be tied to weak, ill-defined coupling at the interface between the polymer matrix and the nanoparticle. Furthermore, insufficient quantification of the often complex hierarchical morphology present in PNCs have hindered detailed comparison of results between laboratories and with theoretical models, thus inhibiting the emergence of general structure-properties relationships for this class of materials.

Characterization of nanocomposite morphology must overcome many significant challenges before these structure-properties relationships can mature. Methods for quantitative morphology characterization can be grouped into four categories: real space (microscopy), reciprocal space (scattering), interfacial area (NMR, optical spectroscopy, dielectric spectroscopy), and physical effects (rheology, mechanical properties, barrier properties).[10] The first (real space) provides a direct view of the morphology; however, care must be taken to avoid artifacts, to interpret images correctly, and to image a statistically significant amount of material. Reciprocal space scattering techniques are extremely powerful and they typically sample large amount of materials, although similar problems with proper data interpretation exist. Spectroscopy techniques such as dielectric and NMR can be sensitive to changes in structure and dynamics at the nanoparticle/matrix interface, and therefore can be used to probe the amount of interfacial area in nanocomposites. The use of physical effects such as mechanical

† Materials and Manufacturing Directorate, Air Force Research Laboratory.
‡ UES Inc.
§ FEI Company.
|| Triune Software.
○ Innovative Management and Technology Services.
Universal Technology Corporation, Dayton, Ohio 45432
* Corresponding author.

10.1021/ma702232f CCC: $40.75
Published on Web 02/23/2008

properties or barrier data to infer morphology is indirect, albeit useful in certain cases.

All of the above characterization techniques suffer from certain limitations. One major limitation is that these methods often require models for interpretation, thus making some assumptions about morphology. It is possible in certain cases for multiple distinct morphologies to result in very similar scattering patterns, dielectric spectra, or mechanical properties, and therefore drawing definitive conclusions becomes difficult. Even real-space imaging of PNCs, which usually involves the determination of a three-dimensional structure of a material from the projection of that structure onto a two-dimensional image plane, requires significant assumptions to be made with regard to the 3D structure during image interpretation. Tomography, the reconstruction of a sample's three-dimensional structure from a series of transmission images taken from different directions, has revolutionized the field of medical diagnostic imaging, it has been a key element in biological research, and recently significant applications in physics, chemistry and materials research have been investigated. Electron tomography, in which a 3D image can be generated with nanometer scale resolution, decreases the amount of assumptions that are made in image interpretation, and is rapidly becoming a valuable analytical technique for 3D imaging of nanostructured materials.[11]

This paper will discuss the details of (automated) tomographic image acquisition of layered silicate PNCs including 3D reconstruction, image segmentation, and image analysis in three dimensions. A 3D fast Fourier transformation (FFT) taken from a tomographic image reconstruction enables quantitative comparison with SAXS data, improving our understanding of the correlation between the techniques and enabling an estimate of the minimum representative volume element associated with SAXS spectra. Electron tomography will be a valuable tool to facilitate structure-properties development of PNCs.

II. Experimental Section

(1) Nanocomposite Processing. Nanocomposites were prepared according to methods described previously.[12] In short, organically modified montmorillonite (OMMT, I.30E, 145 mequiv/100 g, octadecylammonium bromide, NanoCor) was processed into an epoxy matrix (Epon 862, bisphenyl F epoxide) with an aromatic diamine curing agent (Epikure W, Resolution Performance Products). For image contrast calculations, the average atomic number calculated from the Epon 862 monomer structure was 4.1. The average atomic number calculated from the chemical formula of MMT, as given in section III (1), was 9.0. OMMT (3 wt % I30.E) and epoxy monomers were combined via simple dispersion and underwent high-shear mixing as well as probe sonication, with additional two cycles of 30 min mixing and 10 min sonication after addition of the curing agent. Previous work has shown that these two dispersion methods, combined with cryo-compounding techniques, produce well-dispersed montmorillonite in epoxy.[12]

(2) Tilt Series Acquisition. High angle annular dark field scanning transmission electron microscopy (HAADF−STEM) images were acquired using a 200 kV FEG Tecnai Super Twin equipped with both a Gatan imaging filter (GIF) and Fischione HAADF detector. Beam conditions were spot size 8 (STEM mode), 1 s frame time, 100−150 k× magnification. Tilt series were acquired using the Xplore3D software package (FEI Company), collecting one image every two degrees over the range of ± 50°, and one image every degree at tilt angles larger than 50°, for a total angular range of ± 70°. Several HAADF camera lengths were tested for optimum contrast between the layered silicate sheets and the epoxy matrix, and 200 mm was selected (30 mrad inner detector diameter). This distance provides Rutherford scattering from MMT (section III (2)). Cross-correlations were performed between sequential images in the tilt series, and the sample was automatically translated to minimize drift during acquisition.

(3) Image Reconstruction, Processing, and Analysis. Alignment and reconstruction were performed using the Inspect3D software package (FEI Company). Image processing was done primarily using the ITK/VTK toolkit, with visualization in Paraview (Kitware) and Amira (Mercury Computer Systems). Photoshop (Adobe), and Fovea Pro (Reindeer Graphics) were also used for processing of two-dimensional slices from the 3D image reconstruction. Eikona3D (Alpha Tec Ltd) was used for calculation of the power spectrum of the 3D Fast Fourier Transform (FFT), using the "spectrum magnitude" module with the 3D stack of real space images as the input volume for the calculation. The power spectrum magnitude was visualized in Paraview. A Paraview plug-in was written to calculate intensities and statistics of intensity values on the surface of a sphere as a function of the radius of the sphere.

(4) Small-Angle X-ray Scattering. The SAXS data was acquired using a Molecular Metrology system in transmission mode. Integration of the 2D SAXS patterns was done using the FIT2D software package (Andy Hammersly, ESRF).

III. Results and Discussion

Montmorillonite (MMT) is a member of the smectite family of clay minerals consisting of 1 nm thick, hydrophilic aluminosilicate layers that are approximately 100−200 nm in lateral dimension. The general chemical formula for layered aluminosilicates such as mica, MMT and pyrophylite is $[Si_4O_8][Al_2O_2(OH)_2]$, with an octahedrally coordinated alumino-hydroxide layer bound by two tetrahedrally coordinated silica layers. In MMT isomorphic substitution of Al → Mg in the octahedral layer is balanced by positive cations, such as Na^+, in the van der Waals gallery between the layers giving an approximate chemical structure of $Na_{0.4}[Si_4O_8][Al_{1.6}Mg_{0.4}O_2(OH)_2]$. The Na^+ ions on the surface of the alumino silicate layers can be exchanged with organic surfactants to decrease hydrophilicity.

The MMT crystal structure is monoclinic ($C2/m$) with lattice parameters $a = 0.52$ nm, $b = 0.89$ nm, $c = 0.95-1.00$ nm, and $\beta = 95-100°$. Although a three-dimensional unit cell and space group are often quoted for this material, it is generally well understood that the structure lacks long range translational order orthogonal to the layers. In reality the structure is turbostratic, with little or no correlations between stacked layers, other than the c-axis spacing.

(1) Phase-Contrast Imaging. Figure 1a displays a bright-field (BF) TEM micrograph, taken at relatively low magnification of an epoxy/MMT nanocomposite. Note that the experimental setup for BF-TEM and phase-contrast HREM is virtually identical (all that may vary is the size of objective aperture). The image is taken at a large defocus in order to increase contrast from the silicate layers.[13] This is accomplished in practice by tuning the objective lens current in order to focus the lens a certain distance (the defocus value) above the specimen. As with most thermoset/MMT processing formulations the morphology consists of a mixture of individual layers and layer aggregates formed by parallel arrangements of highly swollen layer stacks. There are aggregates up to several microns in size composed of 10 to 100 MMT layers swollen with epoxy to interlayer spacing approximately ranging from 12 to 16 nm. Figure 1b shows a higher magnification BF TEM image taken at a defocus of −200 nm showing several individual MMT layers lying approximately edge on. The imaging conditions for Figure 1, parts a and b, and resulting images, are in general representative of the available literature.[14]

Common artifacts in phase contrast imaging of PLSN include an increase in the apparent silicate layer thickness due to defocus effects, as well as the appearance of Fresnel fringes parallel to the layers,[15] which may mistakenly be interpreted as additional layers.[10] Many studies have used bright-field TEM to character-

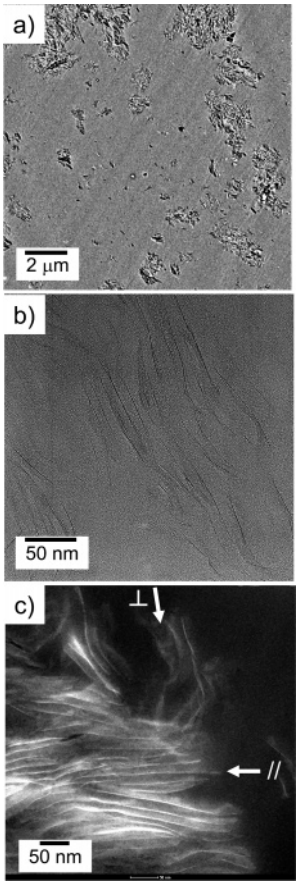

Figure 1. (a) Low magnification bright-field TEM image (Phillips CM200 FEG) of the epoxy/layered silicate nanocomposite. (b) Higher magnification bright-field TEM image of the same nanocomposite taken at an underfocus value of $\Delta d = -200$ nm. The low contrast between the silicate layers and the matrix makes visualization and interpretation difficult in this case. (c) HAADF−STEM image of the same sample, exhibiting excellent contrast between the individual silicate layers and the matrix.

ize layered silicate PNCs in order to evaluate dispersion or other structural factors, and, in general, images from polymer/layered silicate nanocomposites have similar features to Figure 1b, in that a sharp line in the image indicates the presence of a single silicate layer lying parallel to the viewing direction, and a diffuse region of contrast may indicate one or more layers which lie nominally perpendicular to the viewing direction. Phase contrast images depend in a complex manner on sample thickness, defocus, lens aberrations, as well as elemental composition; thus extensive information on the specific imaging conditions is necessary to quantify the detection limit of individual components. Unfortunately, this information is seldom included in the literature.

(2) *Z*-Contrast Imaging. The *Z*-contrast signal, on the other hand, grows exponentially with sample thickness as well as depending on atomic number, *Z*. In HAADF imaging the electron beam is scanned and incoherently scattered electrons are recorded, directly producing images without additional processing.

Figure 1c shows a HAADF−STEM image of a 100 nm thick section of the same nanocomposite, taken on a FEI Super Twin at 200 kV using a 200 mm camera length. Excellent contrast is visible between the individual, 1 nm thick, silicate layers (white lines/sheets) and the epoxy matrix (black background). The contrast in HAADF−STEM goes approximately as the square of the local variation in atomic number,[15] and is free from several artifacts due to specimen thickness or defocus common

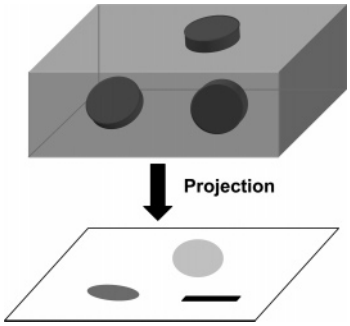

Figure 2. Schematic outlining the changes in projected shape and contrast of thin disks of arbitrary orientation in a 3D matrix onto a 2D image plane.

in both phase-contrast HREM and bright field TEM imaging of layered-silicate PNCs,[10,13,16] which can hinder image interpretation. Figure 1c shows regions where sheets appear to lie perpendicular to the viewing direction (⊥), as well as regions where they appear to lie parallel (||).

The application of tomography techniques gives us access to the third dimension in TEM samples, thus eliminating the need for such qualitative observations. Figure 2 outlines the 2D image interpretation problem in PNCs containing layered nanounits. In particular, the projection of disk-like objects at random orientations onto a plane will produce ellipsoids of varying aspect ratio from a circle to a line with finite thickness. Projection can complicate image interpretation, especially in light of the fact that layered silicate materials rarely have a well-defined lateral geometry.[8] Also conveyed in the figure are the changes in contrast projected for platelets in various orientations. Silicate layers in a plan-view orientation, with their surface perpendicular to the viewing direction exhibit little contrast in projection because of their low thickness in the direction of the beam (∼1 nm).[13] When a silicate layer lies with its surface parallel to the viewing direction, the projected thickness is much greater, because in many cases it will span the entire thickness of the samples, which is on the order of 100 nm.

Figure 3 shows an example of the loss of contrast and definition that accompanies a change in layer orientation with respect to the viewing direction. The figure shows a tilt series of HAADF−STEM images, from 0−20°, along with intensity line scans of the silicate layers in the image (line scans inset, location of scan shown in white directly on the image). The line scan at 0° tilt shows four spikes in intensity corresponding to the presence of four individual silicate layers. As the tilt angle is increased, it is clear that there is a reduction in individual peak intensity as well as peak broadening, and at approximately 20° tilt the individual layers are no longer distinguishable.

There are several implications for this data. The ability to accurately locate an individual silicate layer from a single 2D projection image for segmentation and analysis will be extremely sensitive to the precise orientation of that layer, as the above analysis indicates the loss of individual layer fidelity and contrast at orientational angles of ±15° from the beam direction. Figure 4 shows a schematic of a single silicate layer (thickness *t*, diameter *d*), with arbitrary tilt angle ψ from the direction of the incident radiation, inside of a matrix. The following contrast calculations are valid for the case of the individual layer tilting within a static matrix, shown in Figure 4, as well as tilting of the entire sample, such as the case in tomography. It is of interest to calculate the maximum tilt angle necessary to reduce contrast below an acceptable level, given the relative contrast for MMT and a bisphenol epoxy in HAADF−STEM imaging. Figure 5a displays the projected thickness in the beam direction as a

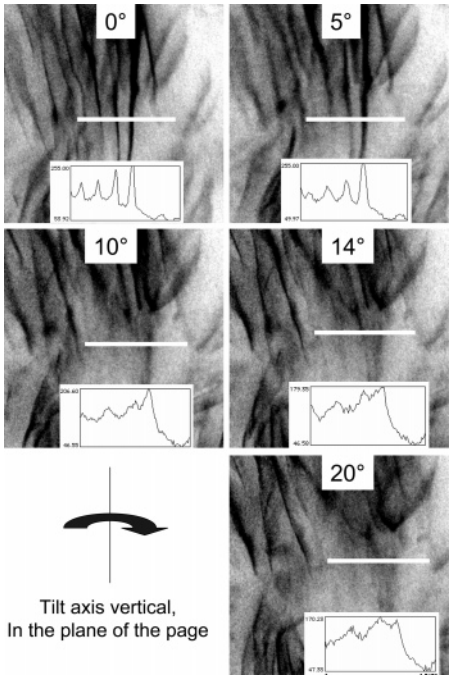

Figure 3. Tilt series in HAADF−STEM imaging mode of a layered silicate nanocomposite. The loss in contrast of the individual layers as a function of tilt angle is represented by the line scans of intensity inset.

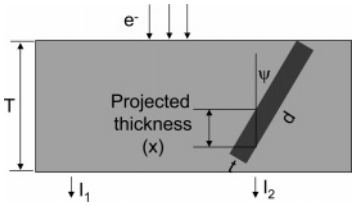

Figure 4. Schematic of the projected thickness of a silicate layer of finite thickness ($t = 1$ nm here) for a given tilt angle from the beam direction, ψ.

function of tilt angle for a three-dimensional silicate layer of lateral dimensions 100 nm and thickness 1 nm, with the effective projected thickness of the matrix in the same region also displayed, assuming a section thickness of 100 nm. The layered silicate projected thickness decreases rapidly with increasing tilt angle ($\sim t/\sin(\psi)$).

When the projected thickness is multiplied by the scattering cross section of the silicate layer, the contrast of that layer inside a matrix of known thickness and scattering cross section can be calculated. The contrast, C, in the image between a region of material containing a single silicate layer (having a scattering intensity of I_2) and a region containing no silicate layers (having a scattering intensity of I_1) is

$$C = \frac{I_2 - I_1}{I_1}$$

where

$$I_1 = \sigma_{mat} I_0 N_{mat} T$$

$$I_2 = \sigma_{sil} I_0 N_{sil} x + (\sigma_{mat} I_0 N_{mat})(T - x)$$

$$x = t/\sin[\psi]$$

x is the effective thickness of the silicate sheet in its projection along the electron beam direction, t is the silicate layer thickness, ψ is the tilt angle of the silicate sheet with respect to the beam direction, σ_{sil} and σ_{mat} is the scattering cross section of the silicate layer and material, respectively, N_{sil} and N_{mat} are the number of atoms per unit volume of the silicate layer and the matrix, respectively, T is the thickness of the section, and I_0 is the intensity of the unscattered beam. The scattering cross section for a HAADF detector assuming Rutherford scattering is[18]

$$\sigma = \left(\frac{m}{m_0}\right)^2 \frac{Z^2\lambda^4}{2\pi^2 {a_0}^2}\left(\frac{\theta_2 - \theta_1}{\theta_1\theta_2\theta'_\alpha} + \frac{1}{\theta'_\alpha}\ln\frac{\theta_1(\theta_2 - \theta'_\alpha)}{\theta_2(\theta_1 + \theta'_\alpha)}\right)$$

where a_0 is the Bohr radius, m is the electron moving mass, m_0 is the electron rest mass, θ_1 and θ_2 are the inner and outer angles of the annular detector, respectively. θ'_α is given by[18]

$$\theta'_\alpha = \sqrt{{\theta_0}^2\left\{1.13 + 3.76\left(\frac{Z}{137(v/c)}\right)^2\right\}}$$

Note that the assumption of Rutherford scattering assumes coherent scattering[17] is neglectable. The Rutherford screening parameter, θ_0, gives the angle above which screening effects of the electron cloud can be ignored and scattering is proportional to Z^2 (Rutherford scattering).[15]

$$\theta_0 = \frac{0.117Z^{1/3}}{E^{1/2}}$$

where Z is the atomic number and E is the energy of the electrons in keV. For $Z = 9$ (approximate average atomic number in the silicate layer) and $E = 200$ kV, $\theta_0 = 17.2$ mrad. The minimum collection angle of the detector used in this study was 15 mrad (30 mrad detector inner diameter), which is slightly less than the threshold for considering only Rutherford scattering. This contribution is minor for these samples and does not alter the subsequent analysis.

Plotting the layered silicate contrast, C, as a function of tilt angle (Figure 5b), we can subsequently determine the detectable limit of contrast for a tilted silicate layer. From the tilt series data we conclude the maximum detectable tilt angle away from the beam direction for a silicate layer is approximately 15°, and therefore from Figure 5b, we see that this value corresponds to a contrast of approximately 17%, which for HAADF−STEM imaging of organic−silicate compositions, corresponds to a reasonable detection limit. Detailed experimental studies of the contrast from many single layers will be necessary to refine this estimate; however the strong variations in contrast with orientation from anisotropic nanoparticles are evident.

This analysis has bearing on the fraction of silicate layers detectable in a single projection image. Silicate layers oriented more than 15° off parallel to the beam direction are not of sufficient contrast to be reliably imaged. Thus, for a single 2D projection image of a randomly oriented nanocomposite, a large portion of the particles will be missed due to the large contrast variations of high aspect ratio nanoparticles. We can calculate the fraction of silicate layers (whose orientation are defined by their surface normal) that fall within 15° from the plane normal to the imaging direction. Silicate layer normals within 15° of this plane are traced out on the surface of a hemisphere in Figure 6a. It is not necessary to consider the lower hemisphere because of the symmetry of an ideal rigid silicate layer; i.e. a negative layer tilt angle is equal to a 180° rotation about the imaging direction and a subsequent positive tilt. The area fraction traced

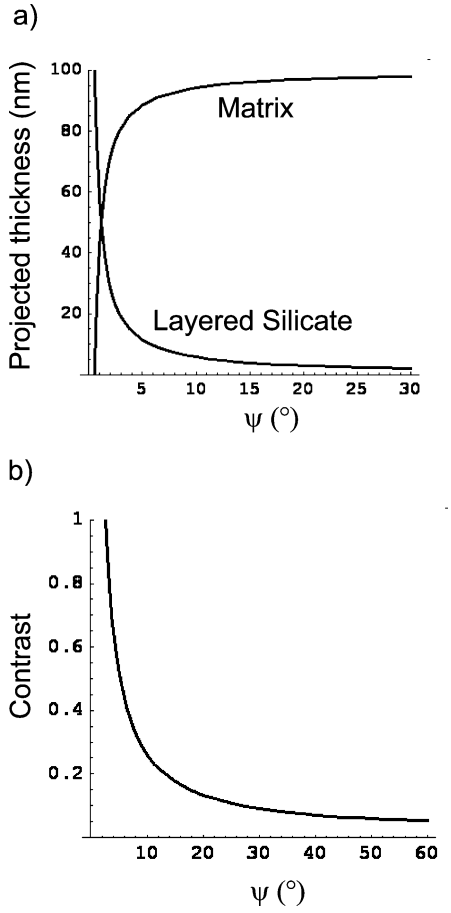

Figure 5. (a) Plot of the projected thickness of the layer (thickness, $t = 1$ nm) and the matrix as a function tilt angle ψ, assuming a constant section thickness (100 nm). The individual layer displaces more matrix material as ψ decreases. (b) Theoretical contrast of one silicate layer ($t = 1$ nm, $d = 100$ nm) with respect to the epoxy matrix as a function of layer tilt angle, ψ (section thickness = 100 nm, $Z_{silicate} = 9.0$, $Z_{matrix} = 4.1$, $\rho_{sil} = 2.25$ g/cm^3, $\rho_{mat} = 1.03$ g/cm^3).

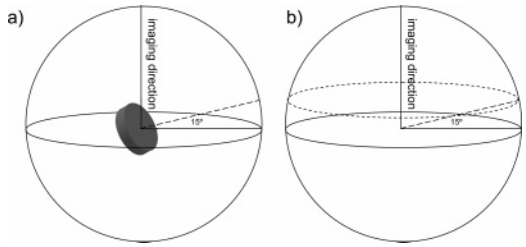

Figure 6. (a) Schematic of all possible silicate orientations, as outlined by the layer normals defining the surface of a sphere. For the case of an ideally flat silicate layer, the symmetry of the layer requires only the top hemisphere needs to be considered. (b) For tilt angles of 15°, a spherical band is traced out whose area is approximately 25% of the top hemisphere.

out by the layer normal vectors of tilt angles 15° or less (Figure 6b), with respect to the area of the entire upper hemisphere, is 25.8%.

Therefore, for a single projection HAADF−STEM image of randomly oriented layered silicate, only about one-quarter of all the silicate layers are detected. Much of this 25% has a increased apparent width (equal to d sin[ψ] in Figure 4), reducing individual layer definition.

(3) Tilt Series and 3D Image Reconstruction. Figure 7 shows snapshots taken from the tilt series at increasing tilt angle, and it is immediately apparent that simply being able to tilt the sample to an angle of 70° improves the understanding of the

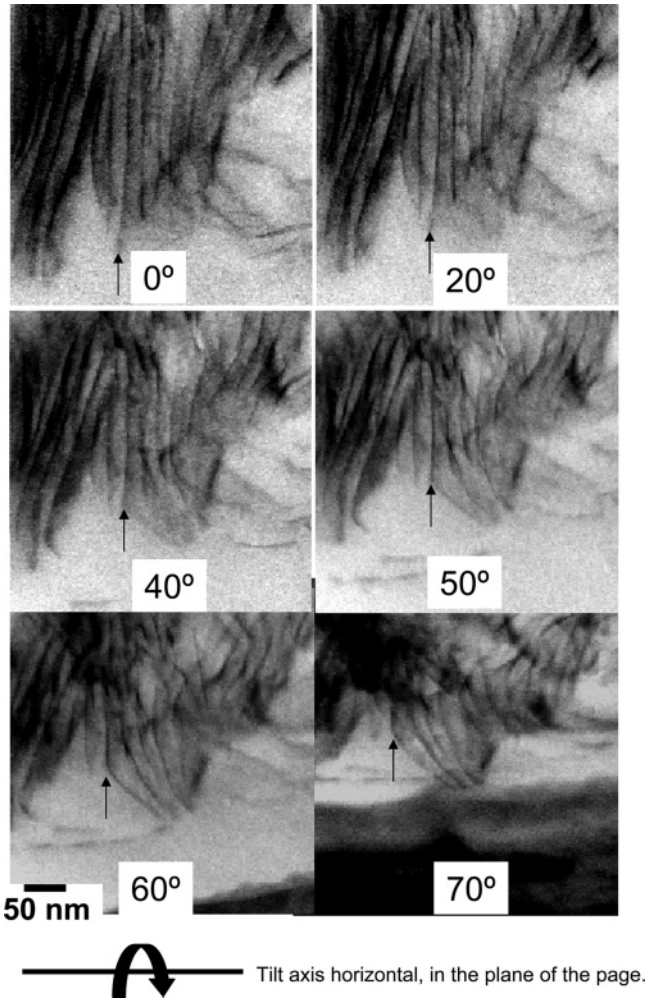

Figure 7. Tilt series of an epoxy/layered silicate nanocomposite collected in HAADF−STEM mode. The tilt axis is horizontal and in the plane of the page. The arrow points to the same sheet in each as a guide to the eye.

local microstructure. The zero tilt image shows several dark MMT layers that qualitatively appear to be running in and out of the plane of the page. When the sample is tilted past approximately 45°, about a horizontal tilt axis, which lies in the plane of the page, the individual layers are observed to coherently bend into the plane of the section. Coherent bending of layered silicates swollen with epoxy has been observed previously,[13] and may occur due to local variations in intra-gallery vs extra-gallery polymerization rates during the curing cycle of the epoxy.[19]

For the tomography reconstruction, we performed a tilt series on a representative area of sample. Images were acquired from ±70°, at 2° increments at tilt angles less than 50° and 1° increments at tilt angles higher than 50°. Two degree increments provided more than adequate resolution in the reconstruction, however at high tilt angle one degree increments ensured proper focusing as well as accurate tracking between images. The cross-correlation method was used for sample position tracking (drift correction) during acquisition of the tilt series. Fiducial markers were not necessary in this case to achieve subpixel alignment accuracy when refining the initial cross-correlation with subsequent rounds of cross-correlation on the already aligned stack. A movie of the tilt series is available in Supporting Information.

Because no tracer particles were used, measurement of section shrinkage during acquisition was difficult. The total electron dose was likely more than the critical dose for taking mont-

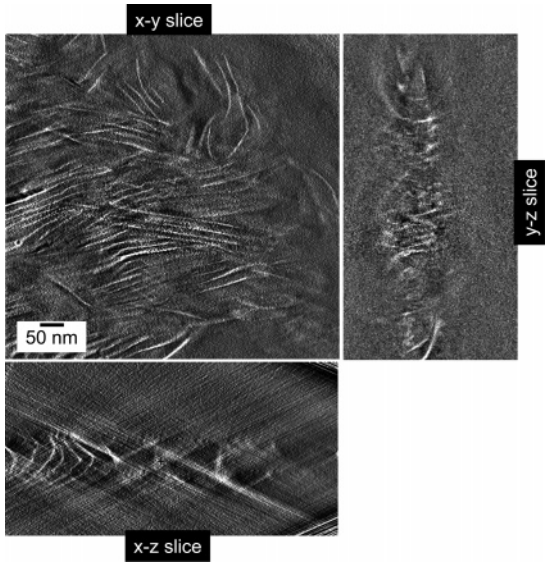

Figure 8. Results of the tomography reconstruction by weighted back projection. Slices along three orthogonal planes are displayed.

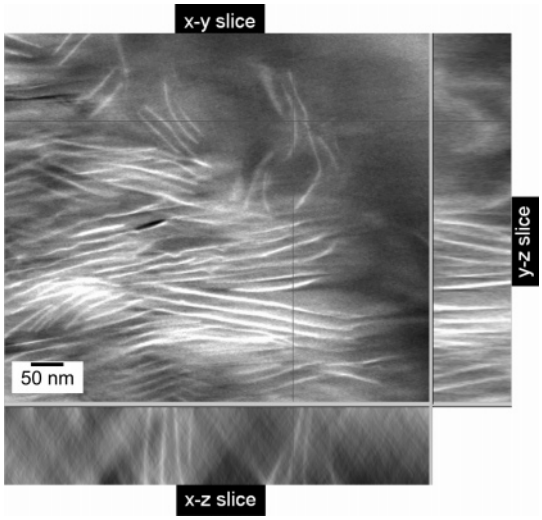

Figure 9. Results of the reconstruction by SIRT. Slices along three orthogonal planes are displayed. The image volume shows an improved signal-to-noise ratio.

morillonite through its crystalline to amorphous transition (100 C/cm^2),[13] however it was less than necessary to produce significant mass loss or shrinkage from the epoxy matrix. Changes in MMT layer morphology are not observed during the crystalline to amorphous transition, and therefore beam damage is not expected to interfere with reconstruction of the MMT layers.

Two different methods (both in Inspect3D) were used to create the reconstruction. The results will be briefly compared here. The weighted back projection method (Figure 8) resulted in adequate contrast and definition of the individual MMT layers in the matrix. Several artifacts were present in the reconstruction, though, including streaking due to the missing wedge and excessive noise, which complicated further processing and segmentation of the features of interest in the data set. The artifacts due to the missing wedge appeared as streaks, which were very similar in gray level and size to the features of interest, the MMT sheets, thus preventing a representative segmentation of the image volume. In contrast, using the simultaneous iterative reconstruction technique (SIRT), shown in Figure 9,[20] the reduction in noise in the data set is readily apparent, and the streaking above and below the section visible in the x-z slice is less pronounced. The slightly uneven sampling of projections (change from 1° to 2° increments) is not expected to cause significant problems in the reconstruction, as the SIRT method has been shown to accurately reconstruct data sets with uneven projection distributions.[21] The SIRT reconstructed data set was suitable for image segmentation and analysis.

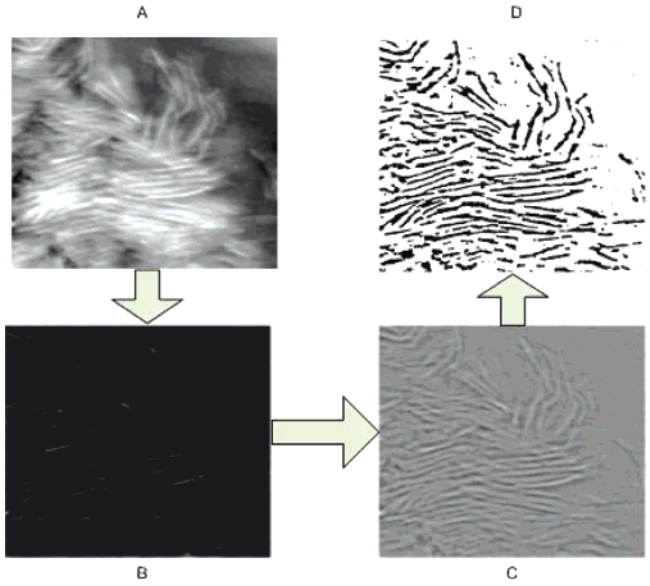

Figure 10. Image processing steps for segmentation: (a) A Gaussian blur and a high pass filter are applied to the image to remove noise as well as long range background intensity variations. (b) An opening filter is used to remove "bridges" and small particles less than a predetermined diameter. (c) An arithmetic Laplacian filter is used to calculate the second derivative of the image, filter out low frequencies, and enhance the boundaries of objects. (d) The image is then contrast enhanced and inverted, and a threshold is applied to produce a binary image.

(4) Segmentation. In computer vision and image processing applications, the term segmentation refers to the partitioning of a digital image into multiple regions or sets of pixels.[22] In order to extract the features of interest (MMT layers) from the background (epoxy matrix) an image segmentation routine was developed, shown in Figure 10. A Gaussian blur and a high pass filter were applied to the image to remove noise as well as long range background intensity variations. An opening filter was used to remove "bridges" and small particles less than a predetermined diameter. An arithmetic Laplacian filter was then used to calculate the second derivative of the image, filter out low frequencies and enhance the boundaries of objects. Finally, the image was then contrast enhanced, inverted and a threshold is applied to produce a binary image.

The final segmented image (Figure 10D), shown directly to right of the original image (Figure 10A), shows an accurate representation of the shape and extent of the layers, with few false positives, such as the small islands produced by excessive noise. The acceptable level of image processing artifacts such as these false positives will vary for a given application. For the FFT analysis shown subsequently, some noise or small islands not corresponding to any real silicate materials in the matrix will not hinder data interpretation. However for measurement of particle size distribution, the presence of small island artifacts would erroneously skew the distribution toward lower values.

By applying this procedure sequentially to all $x-y$ slices in the reconstructed 3D volume, a 3D segmentation is constructed. Although in a single 2D projection image from PNC with

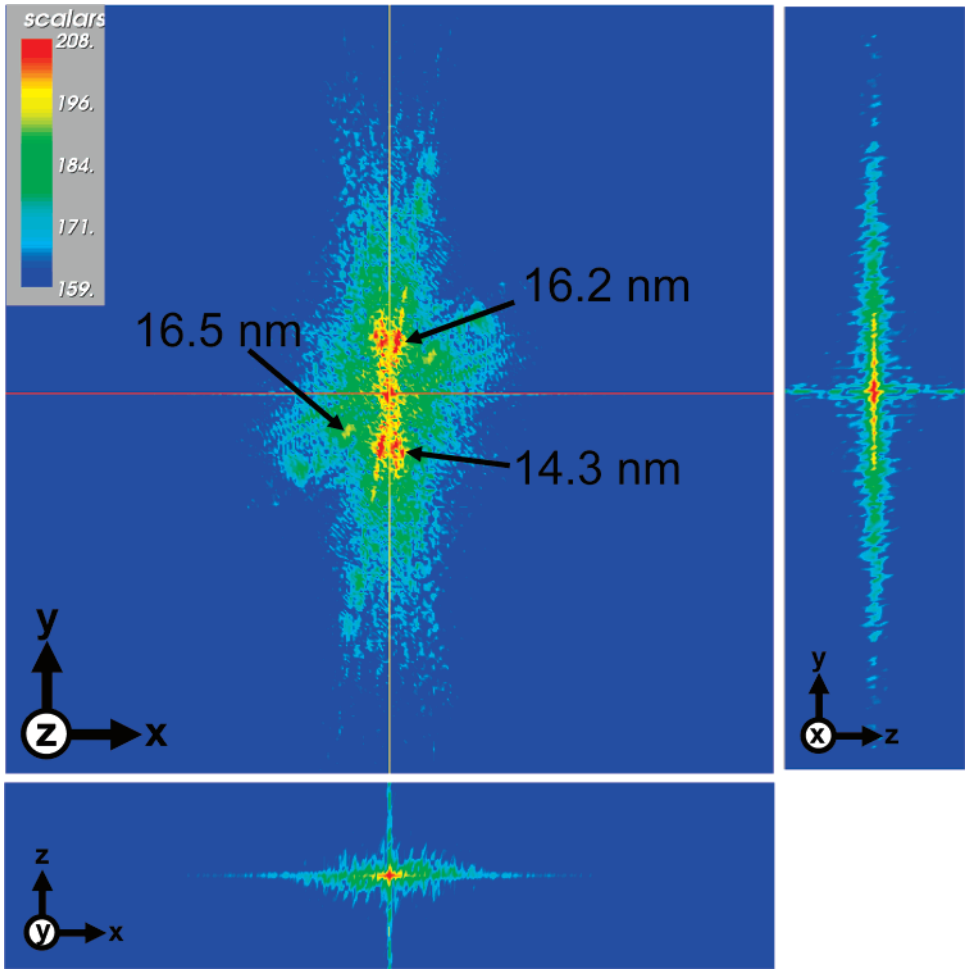

Figure 11. Power spectrum of the 3D FFT. Slices along three orthogonal planes are shown. Several peaks are identified on the *x*−*y* slice, which arise from strong layer−layer correlations in the real-space image volume.

randomly oriented silicate layers we expect to reliably segment only 25% of all layers, because of the ±70 tilt series and subsequent reconstruction, in this case, we expect all layers, regardless of orientation, to be contained in the segmented 3D image.

(5) Morphological Analysis in Reciprocal Space. The calculation of the power spectrum of its Fourier transform is a requirement for quantifying spatial correlations and orientation directly from 2D or 3D images. Features of the power spectrum can be compared to other experimental data in reciprocal space such as small-angle X-ray scattering (SAXS). Microscopic characterization techniques such as TEM provide data that is not always representative of the entire sample. SAXS, on the other hand, probes relatively large volumes of materials, therefore it does not generally suffer from insufficient sampling, and provides a sample size-independent representation of the globally averaged morphology and its associated distributions. For a rough estimate of the volumes of samples probed in each case herein, the local sampling volume of the TEM image and subsequent FFT is $\sim 10^{-1}\ \mu m^3$, where the SAXS data probes a volume of sample $\sim 10^{7}\ \mu m^3$ defined by the beam area and sample thickness. Figure 11 shows the (*x*,*y*), (*x*,*z*), and (*y*,*z*) slices of the power spectrum of the 3D FFT calculated from the segmented volume. These slices all contain the (0,0,0) point of the volume, making them symmetric about the center point. The 3D FFT, shown from orientations along the three major axes, *x*, *y*, and *z*, shows streaking in several directions. This streaking arises from the planar nature of the MMT sheets in real space. The Fourier transform of a plane in 3D real space is a streak normal to that plane. The majority of the MMT layers in the selected image volume lie with their normal nominally in the *y* direction, hence the majority of streaks in the FFT lie near the *y*-axis. Fewer peaks in intensity are visible when looking directly down the *y*-axis of the FFT, as there are relatively few strong interlayer correlations in the image along this axis. Figure 11 shows several primary peaks are visible in the *x*−*y* slice of the FFT, which are labeled on the image at 14.7, 16.5, and 16.9 nm. The peaks in the FFT are directly traceable to subvolume elements exhibiting these measured interlayer spacings.

It is possible to take an intensity line scan of the 3D FFT from the center outward along a certain direction for comparison with SAXS, however the signal-to-noise ratio is low. The 3D FFT can be radially integrated, by calculating the maximum or average intensity value on a sphere centered on the (0,0,0) point of the FFT. The FFT of the original reconstruction before segmentation, shown in the Supporting Information, exhibited artifacts due to the missing data wedge arising from the unobtainable tilt sequence from 70 to 90°. Therefore, a direct comparison between X-ray scattering and FFT intensity was more applicable for the case of the segmented volume. This comparison is described below.

Figure 12a shows the intensity on the surface of a spherical cut of the 3D FFT from the segmented volume. Plotting the integrated intensity as a function of sphere radius, we can display the intensity in the FFT as a function of reciprocal space vector magnitude, in order to directly compare the tomography with SAXS (Figure 12b). A common technique for probing PNC morphology is X-ray scattering, and in many cases both WAXS

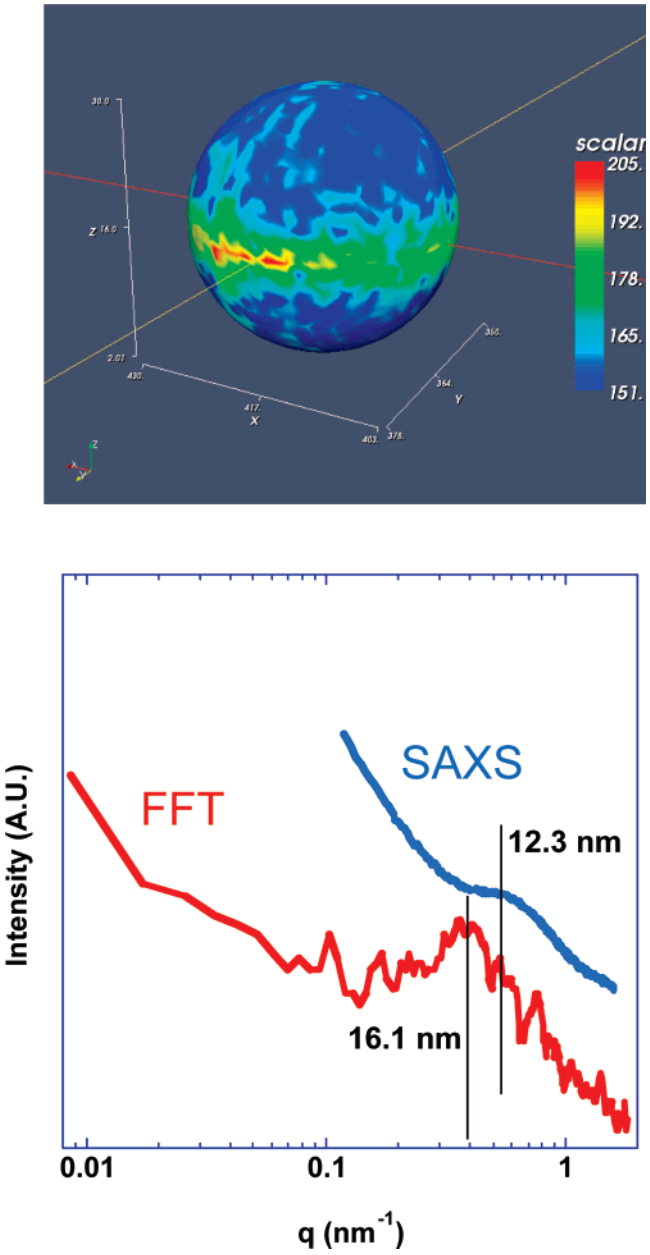

Figure 12. (a) Spherical cut at a defined radius of the 3D FFT power spectrum. (b) Radial integration of the 3D FFT, done by calculating the average intensity on the surface of the sphere as a function of radius, and subsequent normalization of the sphere radius to reciprocal space vector magnitude values, q (red curve). Also plotted on the same axis is the SAXS data from the same sample (blue curve).

and SAXS are necessary to provide sufficient structural information.[23] Both the SAXS and the integrated FFT show a peak, and the peak in the FFT occurs at a slightly lower q value than measured on the SAXS pattern. The data in the FFT extends down to $q \sim 0.01$ nm^{-1}; however, here the sampling is insufficient (essentially one voxel in the FFT is sampled) to provide significant data in low q values. The difference in peak locations for SAXS and the FFT indicates that microstructural features in the sample such as the interlayer spacing are sufficiently heterogeneous on the 1 μm length scale (size of the tomography reconstruction) that the SAXS and FFT will not consistently agree. Thus, individual swollen tactoids, such as those contained in Figure 1a are not adequately representative of the macroscopically averaged distribution of interlayer spacings, let alone coarser features such as layer width or agglomerate distribution. In other words, in this particular example substantially greater tomographic volume ($>10^{-1}$ μm^3) is necessary to fully represent the distribution in local structure.

IV. Summary

A major challenge for the types of analyses presented in this paper is adequate sampling of material using different techniques such as SAXS and electron tomography. For nanostructured materials like PNC, a major advantage of SAXS is that it probes materials with subnanometer resolution and at the same time samples a large number of nanoparticles, thus providing more than adequate statistics. Electron tomography will not be able to analyze similar volumes as SAXS, but the open issue is, what is the sufficient volume?

For the PNC discussed herein, the number of particles analyzed in the electron tomography data, 10^2-10^3, was inadequate. As the minimum sampling volume increases, the dispersion is less ideal and more heterogeneous and the hierarchy of the morphology is greater. Currently, it will be necessary to analyze tomograms from several areas of sample chosen at random, or to stitch multiple tomograms in order to provide a sufficient morphological description. Although these procedures may not yet be routine, the techniques are well within current capabilities. Large-area high-resolution detectors are available that are suitable for tomography (high sensitivity, low acquisition time CCDs), and active efforts are underway to provide automated 2D image acquisition and feature analysis from multiple areas of sample.[24]

While the globally averaged peak contained in the SAXS is also revealed in the integrated FFT, the FFT and the corresponding 3D image volume retain all of the local information which is averaged out in the SAXS data. Reproducible, robust segmentation routines that can be automated, such as described herein, will enable rapid determination of this information, including average domain size, nanoparticle persistence length, local curvature, aspect ratio, and nearest neighbor distribution function. The last parameter, the nearest neighbor distribution of particle centroids, is indicative of the degree of nanoparticle dispersion in the matrix. It is of note that it is not necessary to have one-, two-, or three-dimensional translational order to extract a nearest neighbor distribution from a segmented image. This reflects a separate morphological descriptor of the heterogeneities than that derived from the FFT analysis of interlayer d-spacings, where it is necessary to have translational order in the image. To calculate the nearest neighbor distribution from a 3D tomogram it is necessary to distinguish and identify individual particles and subsequently locate their center of mass or some other descriptor. Several algorithms are available to address this issue, at least in two dimensions,[22a] and it is expected to be a critical development for quantitative PNC tomography and correlation with dispersion-sensitive data such as barrier properties.

The above analysis describes a route to morphology description of PNC through data fusion from multiple characterization techniques. The progress made here, as well as in other recent studies,[11] will provide a portion of the foundation for the processing-structure-properties relationship for PNC to develop. Advancements in several closely related areas will be critical, including the development of statistically accurate morphology models from which properties can be calculated using molecular dynamics, finite element or continuum methods. The morphology models may indeed come directly from three-dimensional real-space data, such as those generated by electron tomography or constructed from quantitative image analysis of a statistically significant data set.

Acknowledgment. The authors acknowledge funding from the Air Force Office of Scientific Research as well as the Air Force Research Laboratory and the AFRL Materials and Manufacturing Directorate. The majority of the research was performed while L.F.D. held a National Research Council fellowship. The authors thank Dr. Hauke Bartsch of Mercury Computer Systems for assistance with visualization.

Supporting Information Available: A movie of the tilt series (.avi file) and a figure showing the three-dimensional power spectrum of the reconstructed volume before segmentation. This material is available free of charge via the Internet at http://pubs.acs.org.

References and Notes

(1) Godovsky, D. Y. *Adv. Polym. Sci.* **2000**, *153*, 163−205.
(2) Osman, M. A.; Rupp, J. E. P.; Suter, U. W. *J. Mater. Chem.* **2005**, *15*, 1298−1304.
(3) a) Lincoln, D. M.; Vaia, R. A.; Brown, J. M.; Benson Tolle, T. H. *Aerospace Conf. Proc. IEEE* **2000**, *4*, 183−192. b) Mallick, K.; Cronin, J.; Arzberger, S. *Proceedings of the Structures, Structural Dynamics, and Materials (48th SDM Conference*); American Institute of Aeronautics and Astronautics: Reston, VA, April, 2006.
(4) (a) Cuisinier, F. J. G.; Steuer, P.; Brisson, A.; Voegel, J. C. *J. Cryst. Growth* **1995**, *1156*, 443−453. (b) Porter, D. *Mater. Sci. Eng., A* **2004**, *365*, 38−45.
(5) Su, X. W.; Zhang, D. M.; Heuer, A. H. *Chem. Mater.* **2004**, *16*, 581−593.
(6) Kröger, N.; Deutzmann, R.; Sumper, M. *Science* **1999**, *286*, 1129−1132.
(7) Polymer Nanocomposites special issue. *MRS Bull.* **2007**, *32*, 314−358.
(8) Grim, R. E. *Clay Mineralogy*, 2nd ed.; McGraw-Hill: New York, 1968.
(9) (a) Ahmadi, S. J.; Huang, Y. D.; Li, W. *J. Mat. Sci.* **2004**, *39*, 1919−1925. (b) Pinnavaia, T. J.; Beal, G. W. *Polymer Clay Nanocomposites*; Wiley: New York 2000. (c) Becker, O.; Simon, G. P. *Adv. Polym. Sci.* **2005**, *179*, 29−82. (d) Manias, E.; Polizos, G.; Nakajima, H.; Heidecker, M. J. In *Flame Retardant Polymer Nanocomposites*; Morgan, A. B., Wilkie, C. A., Eds.; J. Wiley and Sons: Hoboken, NJ, 2007; Chapter 2. (e) Utracki, L. A.; Sepehr, M.; Boccaleri, E. *Polym. Adv. Technol.* **2007**, *18*, 1−37.
(10) Drummy, L. F.; Koerner, H.; Farmer, B. L.; Vaia, R. A. In *CMS Workshop Lectures*, Vol. 15; Carrado, K. A., Bergaya, F., Eds.; The Clay Minerals Society: Chantilly, VA, 2007; pp 97−140.
(11) (a) Weyland, M.; Midgley, P. A.; Thomas, J. M. *J. Phys. Chem. B* **2001**, *105*, 7882−7886. (b) Nishioka, H.; Niihara, K.-I.; Kaneko, T.; Yamanaka, J.; Inoue, T.; Nishi, T.; Jinnai, H. *Composite Interfaces* **2006**, *13*, 589−609. c) Gass, M. H.; Koziol, K.; Windle, A. H.; Midgley, P. A. *Nano Lett.* **2006**, *6*, 376−379. d) Kohjiya, S.; Katoh, A.; Suda, T.; Shimanuki, J.; Ikeda, Y. *Polymer* **2006**, *47*, 3298−3301.
(12) Koerner, H.; Tan, A.; Misra, D.; Drummy, L. F.; Mirau, P.; Vaia, R. A. *Polymer* **2006**, *47*, 3426−3435.
(13) Drummy, L. F.; Koerner, H.; Farmer, K.; Tan, A.; Farmer, B. L.; Vaia, R. A. *J. Phys. Chem. B* **2005**, *109*, 17868−17878.
(14) (a) Malla. P. B.; Robert, M.; Douglas, L. A.; Tessier, D.; Komarneni, S. *Clays Clay Mineral.* **1993**, *41*, 412−422. (b) Vermogen, A.; Masenelli-Varlot, K.; Séguéla, R.; Duchet-Rumeau, J.; Bouchard, S.; Prele, P. *Macromolecules* **2005**, *38*, 9661−9669. (c) Kawasumi, M.; Hasegawa, N.; Kato, M.; Usuki, A.; Okada, A. *Macromolecules* **1997**, *30*, 6333−6338. (d) Eckel, D. F.; Balogh, M. P.; Fasulo, P. D.; Rodgers, W. R. *J. Appl. Polym. Sci.* **2004**, *93*, 1110−1117.
(15) Spence, J. C. H. *High Resolution Electron Microscopy*, 3rd ed.; Oxford University Press: Oxford, 2003.
(16) (a) Ahn, J. H.; Buseck, P. R. *Am. Mineral.* **1990**, *75*, 267−275. (b) Dong, H.; Peacor, D. R. *Clays Clay Mineral.* **1996**, *44*, 257−275.
(17) Langmore, J. P.; Wall, J.; Isaacson, M. S. *Optik* **1973**, *38*, 335−350.
(18) (a) Pennycook, S. J.; Berger, S. D.; Culbertson, R. J. *J. Microsc.* **1986**, *144*, 229−249. (b) Kawasaki, M.; Oikawa, T.; Ibe, K.; Park, K.-H.; Shiojiri, M. *J. Electron Microsc.* **1998**, *47*, 477−488.
(19) a) Lan, T.; Kaviratna, P. D.; Pinnavaia, T. J. *Chem. Mater.* **1995**, *12*, 3376.
(20) Schoenmakers, R. H. M.; Perquin, R. A.; Fliervoet, T. F.; Voorhout, W. *Microsc. Anal.* **2005**, *19*, 9−10.
(21) Sorzano, C. O. S.; Marabini, R.; Boisset, N.; Rietzel, E.; Schröder, R.; Herman, G. T.; Carazo, J. M. *J. Struct. Biol.* **2001**, *133*, 108−118.
(22) (a) Russ, J. C. *The Image Processing Handbook*; CRC Press: Boca Raton, FL. 1998. (b) Shapiro, L. G.; Stockman, G. C. *Computer Vision;* Prentice Hall: Upper Saddle River, NJ, 2001; pp 279−325.
(23) (a) Vaia, R. A.; Liu, W. *J. Polym. Sci., Part B: Polym. Phys.* **2002**, *40*, 1590−1600. (b) Vaia, R. A.; Liu W.; Koerner, H. *J. Polym. Sci., Part B: Polym. Phys.* **2003**, *41*, 3214−3236.
(24) (a) Potter, C. S.; Chu, H.; Frey, B.; Green, C.; Kisseberth, N.; Madden, T. J.; Miller, K. L.; Nahrstedt, K.; Pulokas, J.; Reilein, A.; Tcheng, D.; Weber, D.; Carragher, B. *Ultramicroscopy* **1999**, *77*, 153−161. (b) Suloway, C.; Pulokas, J.; Fellmann, D.; Cheng, A.; Guerra, F.; Quispe, J.; Stagg, S.; Potter, C. S.; Carragher, B. *J. Struct. Biol.* **2005**, *151*, 41−60.

MA702232F